Pusher Propeller and Fuselage Wind Tunnel Testing of a Generic Launched Effects Uninhabited Aerial Vehicle

Luke Battey Aerospace Engineer
Andrew Milligan Aerospace Engineer
Jeffrey D. Sinsay Aerospace Engineer
U.S. Army Combat Capabilities Development Command
Aviation & Missile Center
Moffett Field, CA, USA

ABSTRACT

Aft-mounted, pusher propellers have become commonplace on fixed-wing uninhabited aerial vehicles (UAVs). The U.S. Army has a growing interest in these vehicles, as evident by the Launched Effects (LE) program. An experimental test was completed in the U.S. Army 7- by 10-ft Wind Tunnel at NASA Ames Research Center. A new test apparatus was constructed to evaluate the interactional aerodynamics of a generic LE vehicle fuselage and propeller. Pusher propeller performance data was collected and compared to isolated propeller data collected in the tractor orientation at various rotational speeds, wind speeds and pitch angles. General propeller thrust, power and efficiency trends were found to be consistent with previous works. The installed pusher propeller was found to consistently consume more power than the isolated at the same conditions, but only produced marginally more thrust at low advance ratios. This resulted in a small efficiency deficit for the installed pusher propeller, which decreased with increasing wind speeds. A computational fluid dynamics (CFD) model was created of the test apparatus in both pusher and tractor orientations and exercised at one wind speed and pitch angle. The CFD captured the magnitude of the efficiency well and displayed some of the trends seen in the experimental data.

1. NOTATION

A	Propeller Disk Area (ft^2)
$c(r)$	Propeller Airfoil Chord @ r (ft)
C_T/σ	Propeller Thrust Coef., $T/\sigma\rho A V_{tip}^2$
C_P/σ	Propeller Power Coef., $P/\sigma\rho A V_{tip}^3$
$C_{Qt}, C_{Qt,v}$	Hub (Prop) Torque Tare Coefficients
D_{hub}	Hub (Prop) Drag Tare (lb)
D_{body}	Body Drag Tare (lb)
$f_{e,hub}$	Hub (Prop) Equiv. Flat Plate Drag Area (ft^2)
$f_{e,body}$	Body Equiv. Flat Plate Drag Area (ft^2)
$F_{x,prop}$	Propeller Load Cell Force (lb)
$F_{x,body}$	Body Load Cell Force (lb)
J	Legacy Propeller Advance Ratio
M_x	Propeller Load Cell Moment (in·lb)
N_b	Number of Propeller Blades
O_C	Orientation Correction, 1: Pusher, -1: Tractor
P_{prop}	Propeller Power (ft·lb/s)
P_{SLS}	Sea-Level Power (ft·lb/s)
Q_{prop}	Propeller Torque (in·lb)
Q_{tare}	Hub (Prop) Torque Tare (in·lb)
r	Propeller Partial Radius (ft)
R	Propeller Tip Radius (ft)
$Re_{75\%R}$	Reynolds Number at 75% Prop Radius
Re_{body}	Body Reynolds Number
T_{iso}	Isolated Propeller Thrust (lb)
T_{pusher}	Installed Pusher Propeller Thrust (lb)
T_{SLS}	Sea-Level Thrust, Iso. or Pusher (lb)
v_{ind}	Propeller Induced Velocity (ft/s)
V_{tip}	Propeller Tip Speed (ft/s)
V_∞	Tunnel Air Speed (ft/s)
X_{Qt}	Hub (Prop) Torque Tare Exponent
η	Propeller Efficiency, Iso. or Pusher
$\Theta_{75\%R}$	Propeller Pitch at 75% Radius (º)
μ_{prop}	Propeller Advance Ratio, V_∞/V_{tip}
ν	Kinematic Viscosity (ft^2/s)
ρ	Tunnel Air Density (slug/ft^3)
σ	Solidity, Thrust-Weighted
τ	Propeller Load Cell Temperature (ºF)
Ω_{rpm}	Rotational Speed (rev/min)

Presented at the 50th European Rotorcraft Forum, Marseille, France, 10-12 September 2024.

2. INTRODUCTION

In recent years the use of propellers for aircraft applications has increased, including use as auxiliary propulsion, fixed pitch/variable speed lift propellers and in various UAS configurations. The U.S Army Launched Effects effort is one example of a UAS application as shown in Reference 1. The DoD operates small UAS with fixed pitch propellers, including RQ-11, RQ-21, and RQ-7, and is developing small, fixed wing UAS under the Launched Effects effort. These aircraft have small, rear-mounted pusher propellers. This may present unique interactional aerodynamics and performance characteristics compared to front-mounted (tractor) propellers or isolated propellers more commonly seen in many hobby, historic, and experimental test configurations.

Many sources have experimentally tested and/or collected performance data on small UAS propellers in tractor or isolated as much as practically possible. The widely used UIUC propeller database [Ref. 2] is a vast resource for small diameter propeller data that is still being added to, which attempts to back out isolated propeller data. Other data, also on practically isolated propellers, include the U.S. Army [Ref. 3], NASA [Ref. 4], and other universities [Ref. 5].

Experimental data on propeller-fuselage interaction is not only more limited, but also aircraft and scale dependent. In the 1920's and 30's, the British Aeronautical Research Committee (BARC) tested propeller-body interactions for various axisymmetric bodies [Ref. 6]. NASA tested aft-mounted propellers on airships in the 1960's [Ref. 7], and the effect of pusher propellers on airframe aerodynamic characteristics of a general aviation configuration in the 1980's [Ref. 8]. Pratt and Whitney tested the effect of prop-fan engines in both tractor and pusher [Ref. 9] and saw a slight benefit of tractor, if other component impacts were neglected, for a notional 120 passenger aircraft. Delft University conducted pusher vs. tractor comparisons of a wing-tip mounted propeller pylon [Ref. 10]. The differences seen were expected to be due to interaction with the wing tip vortex, making studies like this less relevant to the present work.

Sikorsky tested isolated and pusher propellers on a helicopter fuselage [Ref 11]. Sikorsky found that their installed pusher propeller efficiency could exceed that of the isolated for low thrust coefficients but decreases at high thrust. It was also theorized that the range of findings in the existing literature are due to differences in body shape, size and propeller design.

While these previous works are insightful, they all use different geometries, sizes/scales, and conditions than of interest here. As such, the performance impacts from a pusher vs. isolated propeller are quantified in this work for a generic propeller and fuselage for small fixed-wing UAS. The objective of this work is to explore some of the conditions that cause differences between isolated and pusher propellers on a fuselage, identifying useful trends and providing experimental data for further validating computational models.

A wind tunnel test model was constructed with a generic fuselage shape and size ahead of a speed-controlled propeller to test installed pusher propeller performance. Data of interest are thrust, power and efficiency while varying wind speed, propeller pitch and rotational speed. The model is turned backwards into the tractor orientation, and a spinner added (absent in the pusher configuration), such that the fuselage becomes a fairing to collect isolated propeller data as a baseline. CAD models of the test model in both orientations are shown in Figure 1.

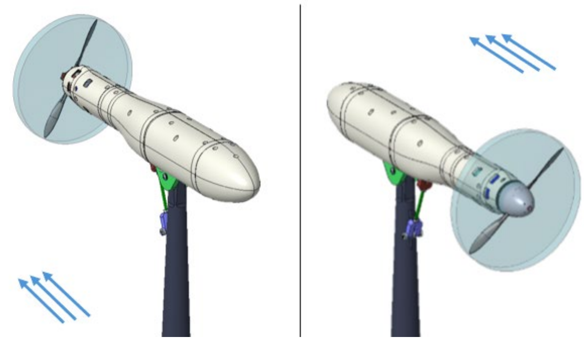

Figure 1. Test model in pusher and isolated modes

3. EXPERIMENTAL SETUP

This section details the hardware, software, techniques, and experience used (and created) to complete the test. This includes details of the facility, test model, instrumentation, control, and lessons learned.

3.1 WIND TUNNEL

The experiment was completed in December 2023 in the U.S. Army 7- by 10-ft Wind Tunnel (2.1- by 3.0-m) located at NASA Ames Research Center in Moffett Field, CA. It is a subsonic, atmospheric, closed-circuit, single-return tunnel with a rectangular test section that measures 7-ft high, 10-ft wide and 15-ft long. The maximum achievable speed in the test section is about Mach 0.3, or 200 kt (103 m/s). The tunnel features a variable RPM fan drive, closable air exchange, and a 13:1 area contraction ratio. The tunnel's data acquisition system is called the Standard Data Acquisition System (SDAS) which manages the collection of atmospheric properties, dynamic pressure, and other test-specific data. The SDAS is connected to the tunnel's built-in turntable and 6-axis scale, which is locked-out for this test because separate load cells are used, detailed in a subsequent section.

3.2 TEST MODEL OVERVIEW

The test model is intended to represent a generic launched effects UAV fuselage and propeller to study their interactional aerodynamics. To get baseline isolated propeller performance, the tunnels turntable is rotated 180-degrees to put the propeller upstream. In this tractor orientation, a nose cone spinner is added, and the fuselage acts as downstream fairings. The model can also change body attitude with a pitch link, but the yaw and pitch are set to 0-degrees for this test.

Figure 2a provides an internal view of the test apparatus with key components identified. Figure 2b shows the model installed in the 7x10 wind tunnel along with key model dimensions and the standard tunnel coordinate system. Two 3-axis load cells mount to the strut assembly and support/measure a strongback assembly, which the 3D-printed fuselage/fairing skin segments mount to. The fuselage skins surround the motor and strongback assembly, covering and maintaining clearance with the top of the strut assembly. The brushless motor mounts to a 6-axis load cell, which is also mounted to the strongback. Details on the various components are provided in the following subsections.

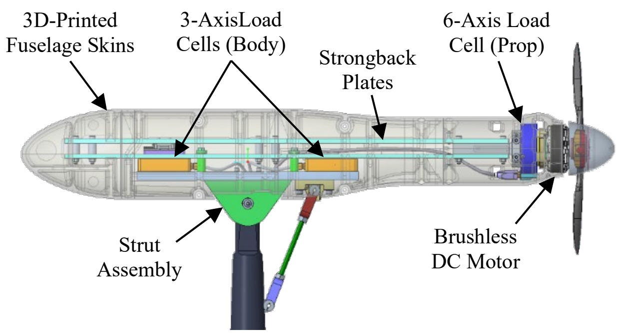

(a) Layout

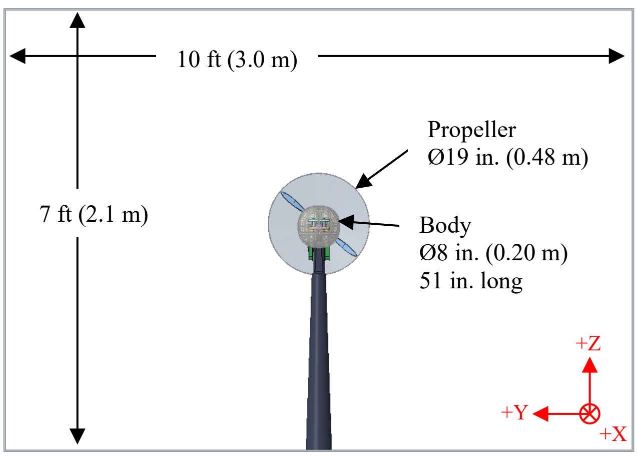

(b) Size in the tunnel

Figure 2. Test model overview

The propeller used (detailed later) is 19 inches (0.48 m) in diameter, being 2.8% of the tunnel's cross-sectional area. The body, from spinner to nose, is 51 inches (1.3 m) long. The widest (and tallest) part of the body is 8 inches.

3.3 Data and Control

Signals of the various components are ultimately transmitted to the SDAS through two ways: 1) a National Instruments CompactDAQ and 2) a Pacific Instruments High Speed Data Acquisition System. Both interface with various LabVIEW Virtual Instruments (VI's) that run on desktop computers in the control room. The VI's interpret signals into engineering units (e.g. lb or ft/s) and one sends command signals through the CompactDAQ to control the model. When the model is on-condition, data from all channels are recorded simultaneously over a specified time range and frequency. Five seconds and 8000 Hz were found to be adequate here. Select channels are recorded as high-speed time-dependent data, while others are time-averaged only. Time-averaged data is added as another row in a separate .csv file that contains every point in the run.

3.4 Body Load Measurement

Two 3-axis force load cells support the strongback and measure what will be referred to as the "body loads", being the force measurements from the "body load cells". The measured body loads include both the aerodynamic forces on the fuselage and the thrust generated by the propeller. This is because the propeller load cell is mounted on the strongback end. As a result, the body loads measurement being derived is the propeller thrust minus the body drag.

Two load cells, as opposed to just one, increase the moment capacity of the test rig. This was desirable due to not knowing the moments caused by the propeller/airframe a priori, and a relatively small moment capacity (and stiffness) of a single load cell. These two load cells, mounted on the strut assembly and with the strongback installed, are shown in Figure 3a and Figure 3b, respectively.

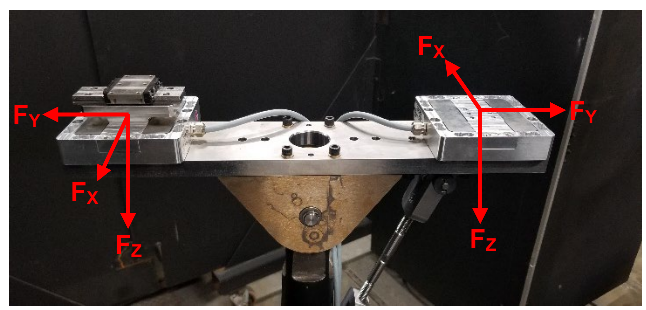

(a) installed on strut

(b) with strongback installed

Figure 3. Body load cells

The nose-side load cell, on the left side in Figure 3a, has a slider mounted on top, consisting of a guide rail and ball bearing carriage. This was done to prevent internal stresses/loads between the load cells that may result from

Approved for public release: distribution unlimited.

the strongback being mounted to both. The result is that most of the force in the thrust/drag direction (y-direction in the load cell coordinate system) is captured by the propeller-side load cell. The nose-side still captures any stiction and is subject to any thermal drift that may occur. The load cells face opposite directions so that thermal drift (or perhaps some other types of measurement errors) from each load cell will tend to cancel-out when the combined reading on both is evaluated. Data for this is provided in the results section.

The body load cells are manufactured by Interface, Inc., model number 3A120 with 112.4 lb (500 N) mechanical ranges in all axes. The measuring ranges are defined as the ranges the load cell is calibrated to and set up to measure. The mechanical ratings are the maximums that the measuring ranges can be set to. Here, the measuring ranges in the x- and y-axis were reduced to 45 lb (200 N) to improve the absolute accuracy. The load cell is advertised as having thermal compensation to minimize drift. The nominal accuracy is specified as ±0.25% of the full-scale measuring range in all axes. The specified accuracy simply serves as a guide when selecting the load cell, rather than a guarantee or accuracy limit. This is because the actual accuracies achievable are case dependent. The load cell specifications are summarized in Table 1.

Table 1. Body 3-axis force load cell ratings

Specification	F_X, F_Y ±lb	F_Z ±lb	Moment ±in·lb
Measuring Range	45	112	-
Mechanical Rating	112	112	-
Overload Rating	337	337	885

Three body load cells (to have one spare) were acquired, which include an amplifier/conditioning box, cables, and custom calibrations. The conditioning box interprets the analog signals from the load cell unit and outputs analog voltages that are proportional to the loads in each axis. High speed time histories of all load cell data are recorded and saved.

3.5 Propeller Load Measurement

One 6-axis force and moment load cell supports the motor and rotating assembly and measures what will be referred to as the "propeller loads". Similarly, this 6-axis load cell will be referred to as the "propeller load cell". The measured propeller loads include the propeller thrust, spinner aerodynamic drag, and motor reaction torque. Propeller loads also include the in-plane forces and hub moments, which are of less interest here. The propeller load cell is shown uninstalled in Figure 4a, and installed Figure 4b.

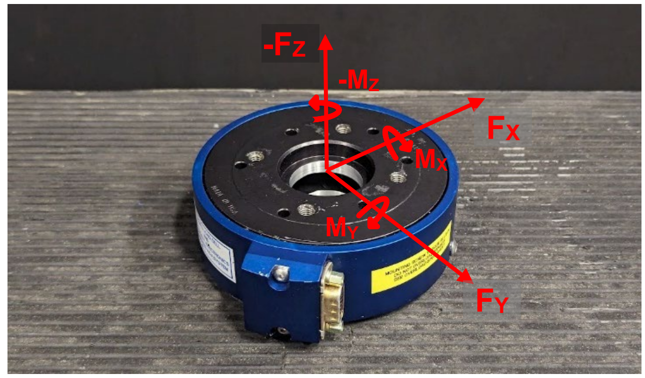

(a) by itself

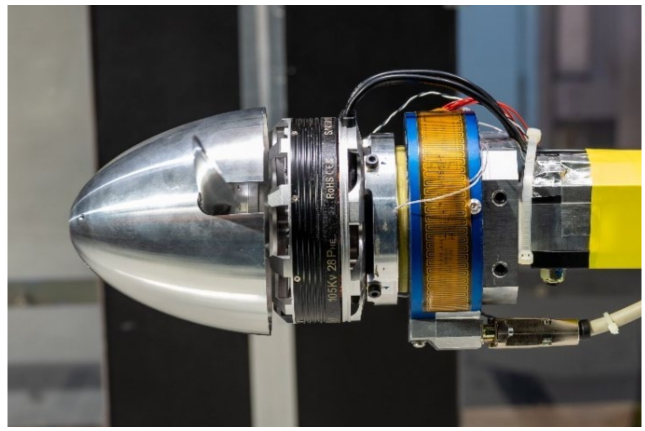

(b) installed in the model

Figure 4. Propeller load cell

The propeller load cell is manufactured by JR3, Inc., model number 45E15-I63-EF-100L, which has analog output and external electronics. This load cell includes the option of two sets of customized electronic measuring ranges, achieved by changing jumpers in the conditioning box to adjust the gains. The jumpers were left on for this entry, making the measuring range 35% of the full mechanical rating. The propeller load cell specifications are summarized in Table 2.

Table 2. Propeller 6-axis load cell ratings

Specification	F_X, F_Y ±lb	F_Z ±lb	M_X, M_Y ±in·lb	M_Z ±in·lb
Measuring Range	35	70	158	158
Mechanical Rating	100	200	450	450
Overload Rating	550	2200	2050	1750

The nominal accuracy is advertised as ±0.25% of the full-scale measuring ranges (%FS), which is again not guaranteed. This load cell is also advertised as having thermal compensation to minimize drift. Two propeller load cells (to have one spare) were acquired, which include an amplifier and conditioning box, cables, and custom calibrations. The conditioning box outputs six analog voltage signals that correspond to the six axes with some cross-coupling. These must be multiplied by a 6x6 calibration matrix (done in LabVIEW) to arrive at de-coupled loads in engineering units.

Before the present test entry, a shakedown test was completed in the wind tunnel to validate the integration of the various components. Results from the propeller load cell showed zero-drift of up to 25 times larger than the specified nominal accuracy, with the thrust load being the most susceptible axis. Steps were taken to insulate the motor heat from conducting into the load cell, as well as cooling it. Post-test thermal corrections were also formulated and applied. However, these fixes only improved the zero-drift to about 5 times the nominal accuracy. Another initial issue was that while the motor was energized, the mean load measurements exhibited offsets which were unexplained by the mechanics of the setup. This was suspected to be electromagnetic interference (EMI), or electrical noise, from the motor affecting the load cells. These problems required fixes to be found before the present entry.

3.6 Load Cell Fixes

A load cell heating strategy was developed to address the thermal drift. Flexible, adhesive backed, resistive heaters were added to the curved surface of the load cell, seen in Figure 4b colored orange, which provide up to 120-watts of heat in total. Thermocouples were placed on the front, measured (sometimes called “metric”) face as well as the rear, un-measured (non-metric) face and on the heating element itself. Because the heaters were placed on an un-measured surface, energizing them would initially heat the rear face more, as the heat would have to conduct through the flexures in the load cell to reach the front face. Conversely, energizing the motor would initially heat the measured face. The amount of resistive heat applied was modulated by the duty cycle of a relay wired to a standard 120VAC plug. Experimentation with this setup revealed that the drift could be most effectively minimized by minimizing the temperature difference between the measured and un-measured faces. This was done with a Proportional-Integral-Derivative (PID) controller in LabVIEW. The average temperature change was then left uncontrolled, but the load cell was already thermally compensated for this, and it could be further improved with post-process thermal corrections. Ultimately, the zero drift in the thrust direction was reduced to about 1.5 times the nominal accuracy, or about ±0.25 lb. However, the drift of the motor torque axis was reduced to ±0.07 in·lb (±0.04% FS), which exceeds the nominal accuracy. While higher accuracy of the propeller load cell thrust would be ideal, it was not required for the findings in this work, because the installed thrust calculation from the body load cell data is ultimately what is used.

The electromagnetic interference, affecting the load cell when the motor was energized, was found to be exacerbated from the motor being grounded to the load cell through its mount. A non-conductive mount was made, which electrically isolated the motor case from all instrumentation. This essentially eliminated the noise and offsets in the load cell data and improved the data quality of other sensors as well.

3.7 Motor and Power Delivery

The motor is a KDE Direct model KDE10218XF-105, which is a brushless direct-current (BLDC) outrunner with a kV of 105 rpm/V. It has a rated power of 7,400 W (up to 142 A) for 180 seconds continuously. It was found to begin overheating at intermediate periods of around 4,800 W and less than half the rated current. The exact values had some dependence on how long it was operated at partial power beforehand, which may have limited the maximum power in practice. The rated power was not attainable even if the fairings and spinner were removed to provide excessive air cooling from the freestream velocity. To monitor motor temperature, a small Resistance Temperature Detector (RTD) was installed directly on the copper windings using a high-temperature epoxy. This gave a near-instant temperature response, opposed to a thermocouple placed on the motor case which lagged the RTD reading significantly. Per the manufacturer, the windings are rated for 240ºC (464ºF) continuously. To provide margin, a winding temperature limit of 150ºC (302ºF) was initially used. However, even this eventually weakened the permanent magnets in one motor. After replacing it, 120ºC (248ºF) was used and no other issues occurred.

The electronic speed controller (ESC) is an Advanced Power Drives UHV-28S-300, powered by a Delta Elektronika SM210-CP-150 DC power supply. These are oversized because space was not an issue as located under the test section. This ESC has an analog “eRPM” output (in magnetic dipoles per revolution), which provided redundant RPM data. Primary RPM measurements were from an optical sensor (Pololu QTR-1A) that reported an analog 1/rev signal using a reflective patch on the motor bell housing. The RPM measurement is input for a LabVIEW PID controller, which adjusts the Pulse-Width-Modulated (PWM) signal input to the ESC to meet an RPM value specified by the operator.

4. DATA REDUCTION

This section describes the post-test techniques and equations used on the data provided by the SDAS, being already time-averaged, filtered, and in engineering units. Shown are data corrections, aero tares, and new parameters for discussion and analysis purposes including non-dimensionalization.

4.1 Load Cell Loads

For the propeller load cell, two parameters are defined to represent average temperature and temperature gradient differences relative to the zeroed load cell, $\Delta\tau_{ave}$ and $\Delta\tau_{grad}$ (ºF), respectively:

$$\Delta\tau_{ave} = \frac{\tau_M + \tau_{UM}}{2} - \frac{\tau_{M,0} + \tau_{UM,0}}{2} \tag{1}$$

$$\Delta\tau_{grad} = \tau_M - \tau_{UM} - (\tau_{M,0} - \tau_{UM,0}) \tag{2}$$

Where τ_M and τ_{UM} are readings from the thermocouples on the measured (metric) and un-measured (non-metric) faces, respectively. The zero subscripts (e.g. $\tau_{M,0}$) denote the temperatures at the time of zeroing the load cell for the run.

The moment, $M_{x,prop}$ (in·lb), on the propeller load cell in the wind tunnel's x-direction (in line with the propeller shaft axis) is:

$$M_{x,prop} = -O_C \left(M'_{x,prop} - \frac{dM_x}{d\tau_{ave}} \Delta\tau_{ave} \right) \tag{3}$$

Which applies an orientation correction, O_C, to resolve the sign change in the load cell's coordinate system ($M'_{x,prop}$) that results from changing between tractor and pusher orientations:

$$O_C = \begin{cases} -1 & tractor \\ 1 & pusher \end{cases} \tag{4}$$

Eq. (3) also applies a thermal correction using the average temperature delta defined above. The slopes for all the thermal corrections applied are:

$$\frac{dM_x}{d\tau_{ave}} = 0.020 \ \frac{in \cdot lb}{°F} \tag{5}$$

$$\frac{dF_x}{d\tau_{ave}} = 0.040 \ \frac{lb}{°F} \tag{6}$$

$$\frac{dF_x}{d\tau_{grad}} = 0.30 \ \frac{lb}{°F} \tag{7}$$

Which are derived using best-fit lines through data having known loads (mostly at no load) and a wide variety of temperature deltas. The moment's thermal drift dependence on $\Delta\tau_{grad}$ was found to be negligible, hence the absence of that slope.

Similarly, the force, $F_{x,prop}$ (lb), on the propeller load cell in the thrust direction is found as:

$$F_{x,prop} = O_C \left(F'_{x,prop} - \frac{dF_x}{d\tau_{ave}} \Delta\tau_{ave} - \frac{dF_x}{d\tau_{grad}} \Delta\tau_{grad} \right) \tag{8}$$

Which has thermal corrections for both $\Delta\tau_{ave}$ and $\Delta\tau_{grad}$. The latter, $\Delta\tau_{grad}$, was typically much smaller in the test due to the load cell heaters driving it to zero.

The total force acting on the body in the wind tunnel's x-direction is $F_{x,body}$ (lb). This includes the body drag, hub drag and propeller trust, and is found by:

$$F_{x,body} = O_C (F'_{x,body1} - F'_{x,body2}) \tag{9}$$

Where $F'_{x,body1}$ and $F'_{x,body2}$ are the force readings from the individual body loads cells. Since they face opposite directions, a body force in that axis makes one reading negative, hence the subtraction in Eq. (9). This subtraction also tends to cancel-out thermal drift that occurs on the individual load cells (shown later), which is already minimal due to their distance from the motor.

4.2 Isolated Thrust

The isolated propeller thrust T_{iso} (lb), and other corresponding data, are captured with the model in the tractor orientation and serve as a baseline in relation to the pusher propeller. T_{iso} can be derived from the load cell measurements in two ways:

$$T_{iso} = F_{x,prop} + D_{hub,t} \tag{10a}$$

$$= F_{x,body} + D_{body,t} \tag{10b}$$

Where $D_{hub,t}$ and $D_{body,t}$ (lb) are the drag of the propeller hub and entire body (including the hub), respectively, in the tractor orientation. The drag values must be added to the load cell measurements to find the thrust of the propeller blades, because the load cells measure the sum of that thrust minus the drag. These two approaches, (10a) and (10b), provide redundant thrust measurements by using the various load cells on the model.

The tractor hub drag in Equation (10a) is found with the dynamic pressure:

$$D_{hub,t} = f_{e,hub,t} \frac{1}{2} \rho V_\infty^2 \tag{11}$$

$$f_{e,hub,t} = 0.029 \ ft^2 \tag{12}$$

Where ρ (slug/ft^3) and V_∞(ft/s) are the wind tunnel's air density and axial freestream velocity, respectively. The tractor hub's equivalent flat plate drag area, $f_{e,hub,t}$ (ft^2), is found as a best fit using a variety of data at different wind speeds collected with the model in tractor orientation with no blades installed.

The tractor body drag, $D_{body,t}$ (lb), in Equation (10b) can be found in two ways:

$$D_{body,t} = -(F_{x,body} - F_{x,prop}) + D_{hub,t} \tag{13a}$$

$$= f_{e,body,t} \frac{1}{2} \rho \left(V_\infty + 2v_{ind} \left(\frac{V_{\infty,ref}}{V_\infty} \right)^{0.8} \right)^2 \tag{13b}$$

Where Eq. (13a) can be derived by subtracting Eq. (10a) from (10b). However, finding T_{iso} with this $D_{body,t}$ is not a unique solution using $F_{x,body}$, because substituting Eq. (13a) into Eq. (10b) creates Eq. (10a) by definition.

The body drag is influenced by both the freestream velocity and the induced inflow. To find the isolated thrust, T_{iso}, using $F_{x,body}$ uniquely, both velocity components must be accounted for in the body drag tare, which is done using the semi-empirical Equation (13b). This uses an induced inflow calculation, v_{ind} (ft/s), that can be derived from momentum theory (excluded here for brevity, but can be found in rotorcraft aerodynamics texts such as Reference 12):

$$v_{ind} = -\frac{V_\infty}{2} + \sqrt{\left(\frac{V_\infty}{2}\right)^2 + \frac{T_{iso}}{2\rho A}} \tag{14}$$

A (ft^2) is the propeller swept area. The effect of v_{ind} is corrected using with a reference velocity, $V_{\infty,ref}$ (ft/s):

$$V_{\infty,ref} = 118.15\ \frac{ft}{s}\ \ (70\ kt) \tag{15}$$

The body's equivalent flat plate drag area, $f_{e,body,t}$ (ft^2), is:

$$f_{e,body,t} = 0.075\ ft^2 \tag{16}$$

Which is found with tare data in the same manner as the hub drag. The entirety of (13b) can be validated by using the data to compare it to (13a), which provides the empirical part of this semi-empirical drag tare.

4.3 Pusher Thrust

The installed pusher thrust, T_{pusher} (lb), and other corresponding data, are captured with the model in the pusher orientation, and calculated slightly differently than above:

$$T_{pusher} = F_{x,body} + D_{body,p} \tag{17}$$

$$D_{body,p} = f_{e,body,p}\frac{1}{2}\rho V_\infty^2 \tag{18}$$

$$f_{e,body,p} = 0.088\ ft^2 \tag{19}$$

With the body drag, $D_{body,p}$ (lb), calculated using the equivalent flat plate drag area, $f_{e,body,p}$ (ft^2), found with the tare data for the pusher orientation (sans blades).

Here, the installed pusher propeller thrust is defined as the net added thrust to the vehicle, meaning it would include the body drag increment resulting from adding the propeller and the propeller's thrust. This will later result in a net efficiency for the installed pusher propeller case to provide a wholistic comparison with the baseline isolated propeller data. Net thrust and net efficiency are considered standards for evaluating pusher propeller performance, also discussed in References 7, 11 and 13. For discussion purposes, the total body drag of the pusher configuration can be calculated similarly to the tractor:

$$D_{body,p,i} = -\left(F_{x,body} - F_{x,prop}\right) \tag{20}$$

Which excludes a hub drag in the pusher orientation that was found to be negligible being behind the body.

4.4 Torque and Power

The torque produced by the propeller blades, Q_{prop} (in·lb), is found with:

$$Q_{prop} = M_{x,prop} - Q_{tare} \tag{21}$$

The torque tare, Q_{tare} (in·lb), is subtracted from the load cell measurement which measures the propeller blade torque plus the hub/spinner/motor friction torque. Q_{tare} is found with an empirical model. This model and its coefficients (C_{Qt}, C_{Qtv}, and X_{Qt}) are based on data collected whilst spinning the entire rotating assembly minus the blades at various rotational speeds, Ω_{rpm} (rpm), and wind speeds in both pusher and tractor orientations.

$$Q_{tare} = \left(C_{Qt} + C_{Qt,V}\sqrt{\frac{1}{2}\rho V_\infty^2}\right)\left(\frac{\Omega_{rpm}}{1000}\right)^{X_{Qt}} \tag{22}$$

$$tractor\colon \begin{cases} C_{Qt} = 0.030 \\ C_{Qt,V} = 0.0034 \\ X_{Qt} = 1.1 \end{cases},\quad pusher\colon \begin{cases} C_{Qt} = 0.018 \\ C_{Qt,V} = 0 \\ X_{Qt} = 1.5 \end{cases} \tag{23}$$

The propeller power, P_{prop} (ft·lb/s), is found as the product of torque and rotational speed, minding the units:

$$P_{prop} = \frac{Q_{prop}}{12}\frac{\Omega_{rpm}\pi}{30} \tag{24}$$

4.5 Sea-Level Standard Thrust and Power

When plotting dimensional thrust and power, T_{SLS} (lb) and P_{SLS} (ft·lb/s) are used to correct for differences in air density:

$$T_{SLS} = T\frac{\rho_{SLS}}{\rho} \tag{25}$$

$$P_{SLS} = P\frac{\rho_{SLS}}{\rho} \tag{26}$$

Where ρ_{SLS}=0.00238 (slug/ft^3) is the air density at sea-level-standard. T and P are whichever thrust and power are being evaluated, respectively. ρ is the actual air density recorded. These equations are useful because the various runs occur at different tunnel temperatures (and densities).

4.6 Non-Dimensionalization

From the chord-radius distribution, $c(r)$ (ft), the thrust-weighted solidity, σ, is calculated with:

$$\sigma = \frac{3N_b}{\pi R^4}\int_{r_{root}}^{R} c(r)r^2 dr \tag{27}$$

N_b is the number of propeller blades, R (ft) is the rotor tip radius, and r (ft) is a mid-span radius. The root cutout as a percentage is r_{root}/R (%).

Since propellers are, in fact, rotors: generalized rotorcraft-aerodynamics non-dimensionalizations are used here, consistent with those found in Reference 12. This means the axial advance ratio, μ_{prop}, is defined as the ratio of the rotor tip speed, V_{tip}=ΩR (ft/s), to the freestream velocity:

$$\mu_{prop} = \frac{V_\infty}{V_{tip}} \tag{28}$$

The coefficients of thrust and power divided by solidity (a.k.a. blade loading and power-blade loading), C_T/σ and C_P/σ, respectively, are defined as:

$$\frac{C_T}{\sigma} = \frac{T}{\sigma\rho A V_{tip}^2} \tag{29}$$

$$\frac{C_P}{\sigma} = \frac{P}{\sigma\rho A V_{tip}^3} \tag{30}$$

If the legacy, propeller-specific coefficients (dubbed J, $C_{T,J}$ and $C_{P,J}$ here) must be used, they are proportional to Equations (28) – (30) with the following:

$$\mathrm{J} = (\mu_{prop})\pi \tag{31}$$

$$C_{T,J} = \left(\frac{C_T}{\sigma}\right)\frac{\sigma\pi^3}{4} \tag{32}$$

$$C_{P,J} = \left(\frac{C_P}{\sigma}\right)\frac{\sigma\pi^4}{4} \tag{33}$$

Equations (31) – (33) are included for reference only and will not be used in this work.

Note that regardless of which of these sets of coefficients are used, they are not linearly proportional with thrust, power, and wind speed if V_{tip} also changes. This may make plots of these parameters less intuitive for speed-controlled rotors compared to fixed-speed rotors.

The propeller Reynolds number, $Re_{75\%R}$, used here for discussion purposes, is taken at 75% radius:

$$Re_{75\%R} = \frac{c(0.75R)\sqrt{(0.75V_{tip})^2 + V_\infty^2}}{\nu} \tag{34}$$

This includes both rotational and freestream velocity components. $c(0.75R)$ (ft) is the blade chord at 75% radius and the air's kinematic viscosity is ν (ft^2/s).

The body's Reynolds number, Re_{body}, is found using its overall length, L_{body}=4.25 ft, and calculated as:

$$Re_{body} = \frac{L_{body}V_\infty}{\nu} \tag{35}$$

Finally, the propeller efficiency, η, is defined as:

$$\eta = \mu_{prop}\frac{C_T}{C_P} = \frac{TV_\infty}{P} \tag{36}$$

5. PROPELLER

The present propeller consists of two "VarioPROP 456-16 CFK-Propellerblade SG" (VP 456-16 SG) blades installed on a custom hub, the same as used in Reference 14. VarioPROP makes commercial, injection molded, chopped carbon blades with a root end design that allows for ground adjustment of the collective pitch. A high-resolution laser scan of the blade was outsourced to obtain a CAD model with a target accuracy of ±0.001 inches (±0.025 mm) to the physical blade, shown in Figure 5a.

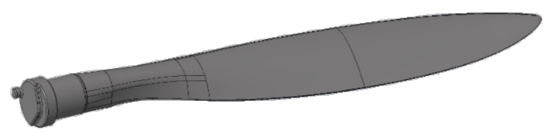

(a) VP 456-16 SG blade

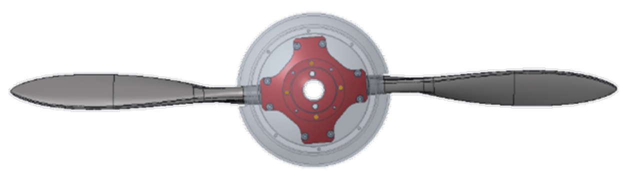

(b) Propeller

Figure 5. Propeller CAD models

This model as installed on the custom hub, shown in Figure 5b, was measured to define the geometry here, including some high-level parameters in Table 3:

Table 3. Propeller parameters

Tip Radius, R	0.792 ft, 9.5 in (0.241 m)
Root cutout, r_{root}/R	35%
Solidity (t.w), σ	0.063
Chord at 75%R, $c_{75\%R}$	0.106 ft, 1.267 in (0.0322 m)
Twist, non-linear	-25º
Collective, $\theta_{75\%R}$	25º, 30º, and 35º
Max Rot. Speed, Ω	733 rad/s, 7000 rpm
Max Tip Speed, V_{tip}	580 ft/s (177 m/s)

Note that the custom hub increases the radius slightly beyond the off-the-shelf version. The root cutout is defined here as the start of the aerodynamic portion of the blade, with the portion inboard transitioning into a circular cross section that interfaces with the hub.

The twist distribution and planform are shown in Figure 6a and Figure 6b, respectively:

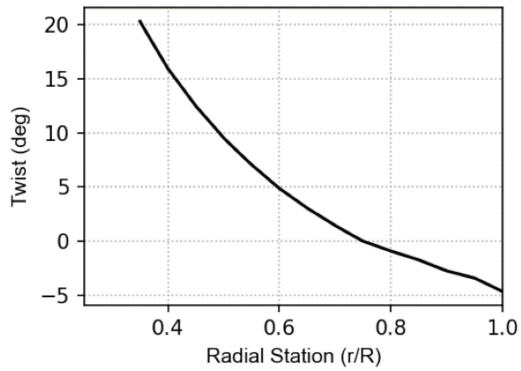

(a) Blade twist

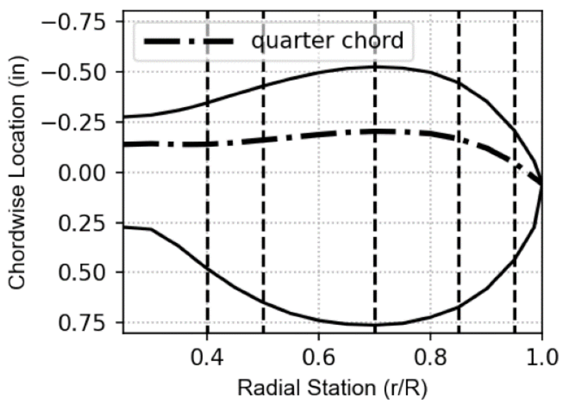

(b) Blade planform

Figure 6. Propeller geometry

The twist fits an inverse tangent distribution (that's been shifted to show 0-degrees at r/R=0.75) except for the outermost 5% and root.

The outer 15% of the blade quarter-chord is swept aft by 8º. Overall, the tip is swept back from the feathering axis by 5º

Figure 7 shows the airfoil cross-sections of the blade, which have a continuous variation in thickness and shape along the radius. Five sections are highlighted that correspond to the spanwise positions identified with vertical dashed lines in Figure 6b.

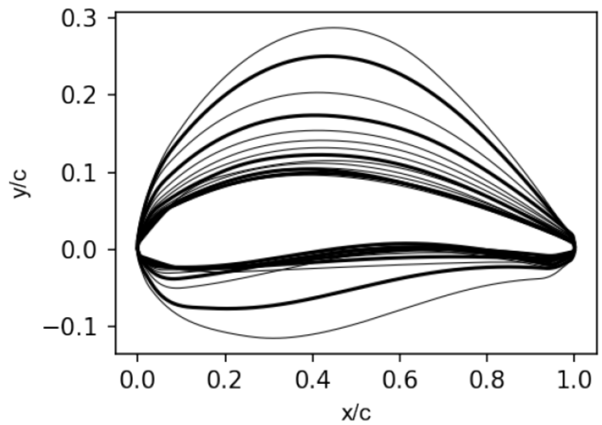

Figure 7. VP 456-16 SG blade airfoil cross-sections, highlighted sections = dashed stations in planform

The collective pitch, being the angle that the 75% span chord line makes with the plane of rotation, was set to three different values during the test: $\theta_{75\%R}$ = 25º, 30º and 35º. A fixture was constructed to set the collective pitch, shown in Figure 8:

Figure 8. Setting the collective pitch angle at 75% radius (tractor orientation)

Here, a digital pitch gauge, Align AP800, is positioned at 75% radius using a custom part that mounts to the top of the hub. The pitch gauge is held on the blade with spring loaded catches that locate the leading and trailing edges. Once the blade is adjusted, the bolts in the shaft-collar-style hub are tightened down to lock it. Then the hub is re-installed on the motor, followed by the spinner (if in tractor mode). For pusher mode, the blade is flipped upside-down when setting the pitch and no spinner is used.

6. EXPERIMENTAL RESULTS

This section provides the conditions tested in the wind tunnel, with corresponding data from tares, corrections, validation data, results and findings for discussion.

6.1 OVERVIEW

The test matrix for the data to be shown is provided in Table 4. Certain wind speeds tested are grayed out for which data will be omitted. These areas are considered out of the propeller and test rigs operating envelope and do not add to the overall findings reported later.

Table 4. Abbreviated Test Matrix

Config.	$\theta_{75\%R}$ (deg)	Tunnel Speed (knots)	Advamce Ratio* $\mu_z = V_\infty / V_{tip}$
Tractor & Pusher	25	30, 50, 70, 90	0.350 - 0.112
	30	30, 50, 70, 90, 110	0.433 - 0.196
	35	50, 70, 90, 110, 130	0.525 - 0.277

The advance ratio ranges given are estimated to provide data between zero thrust and beyond stall. They are typically discretized into 12 equally spaced values to determine the RPM set points. A single run consists of a wind speed and pitch angle. Data is taken in steps, incrementally increasing the RPM to its maximum. After the maximum, the RPM is decreased, and data is taken in fewer steps than when increasing. The lower and upper RPM bounds may be limited by zero thrust and maximum power, respectively.

Pictures from the test in both configurations, pusher and isolated, are shown in Figure 9 and Figure 10, respectively:

Figure 9. Pusher propeller model in the wind tunnel

Figure 10. Isolated propeller model in the wind tunnel

6.2 SETUP & VALIDATION DATA

Figure 11 shows the propeller load cell moment data captured during the final zeros of each run, being taken after the wind and rotational speeds are returned to zero. This is plotted against the load cell average temperature delta, Equation (1), and a best fit slope is overlaid which represents the thermal correction to be applied. After applying the thermal correction, the final moment data (ideally zero) are within ±0.07 in·lb.

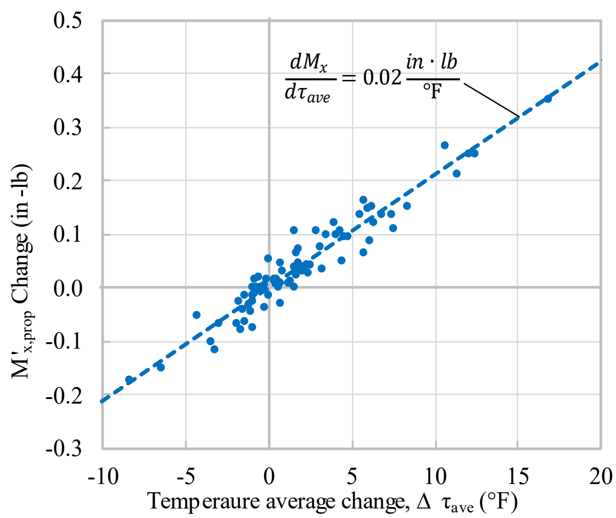

Figure 11. Propeller load cell moment zero drift

Similarly, Figure 12 shows the body load cell thrust measurement from both single body load cells and the combined body load cell measurement, calculated by Equation (9). With no thermocouples on these load cells, this data is plotted against the tunnel temperature change during the run and a weak correlation is seen. The individual body load cells show drift of up to ±0.20 lb. After combining the individual body load cell data per Equation (9), the body load cell data are within ±0.03 lb.

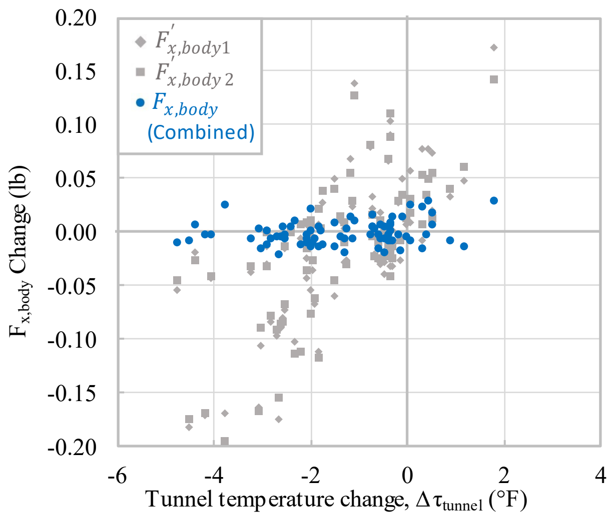

Figure 12. Body load cell force zero drift

The body drag in the tractor orientation with the 30° collective propeller installed is shown in Figure 13, plotted against the isolated thrust. The points represent data calculated using Equation (13a), while the dotted lines are the body drag tare model given in Equation (13b). Drag values from the model are used to subtract from the body load measurement to find the isolated thrust. The data in this example given represents both the highest quality fit achieved (50 kt) and the lowest quality (90 kt). Recalibrating the model to fit this 90 kt data better was attempted as a check, and the resulting thrust does not change enough to alter the findings significantly.

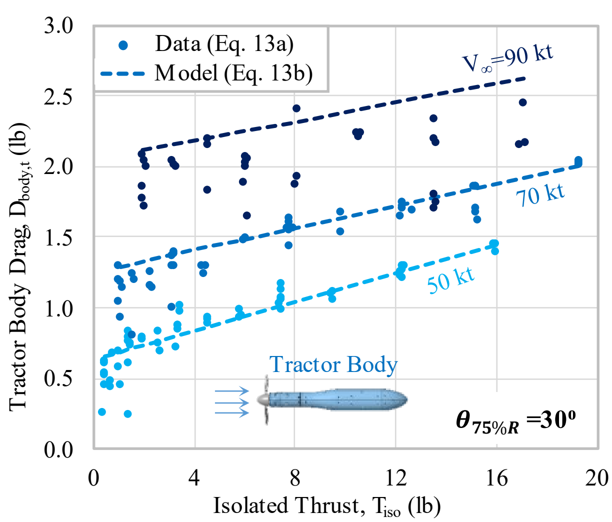

Figure 13. Tractor body drag with thrust

Isolated thrust data for the 30° collective propeller is plotted against rotational speed in Figure 14. The grey square points represent data from the propeller load cell, Equation (10a), while the colored circular points show isolated thrust data from the body load cell data, Equation (10b). The solid lines are moving averages of the body load cell data.

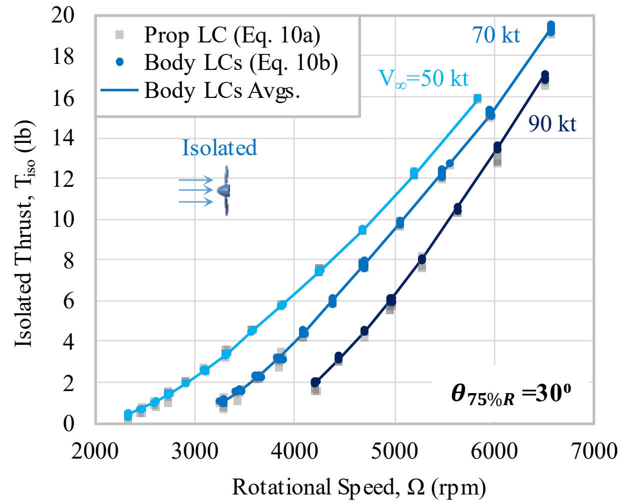

Figure 14. Isolated thrust from both load cell types

Figure 15 shows the blade loading, calculated from Equation (29), of the isolated propeller with the same data as in Figure 14. This highlights the overall agreement between both methods of calculating isolated thrust. Much of the data at higher RPM (and thrust) values are nearly indistinguishable between the two methods. Here, the propeller load cell provides higher quality data, i.e. less scatter, than at lower thrust where significant scatter is observed. Data from the body load cell is higher quality throughout the entire thrust range, which is a motivation for using it exclusively going forward.

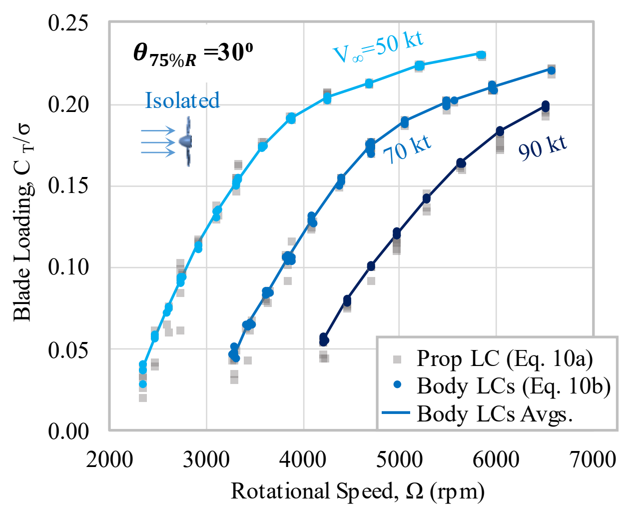

Figure 15. Isolated C_T/σ from both load cell types

The drag of the body in both pusher and tractor orientations, without the blades installed, is shown in Figure 16 plotted against the tunnel speed. The Reynolds number is also included at 50 kt, which increases linearly with the wind speed. Additionally, the pusher body has trip dots installed to force transition at about three inches behind the tip of the nose. The data is shown as points, which are collected in abundance at each speed with and without the motor spinning. The models (best-fit flat plate drag areas) are shown as dashed lines. For the pusher body, this drag model is used as a tare when calculating installed pusher propeller thrust. For the tractor body, the drag model corresponds to the drag at zero thrust in Figure 13.

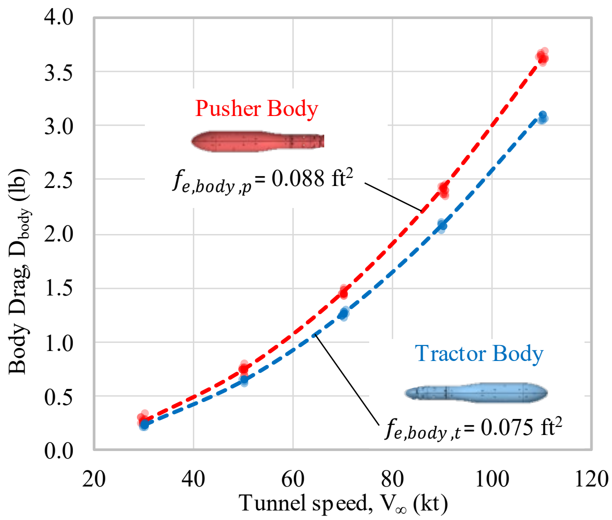

Figure 16. Pusher and tractor body drag tares

The hub torque (inclusive of the hub, spinner and motor torque) for the tractor orientation with the blades uninstalled is shown plotted against RPM in Figure 17. The points are data, and the dashed lines are the model described by Equation (22). While the tractor hub torque displays some dependence on wind speed, the pusher hub (not shown) does not. Both are captured using the coefficients in Equation (23). The torque tare model's value is subtracted from the load cell torque to calculate the torque of the propeller blades alone, per Equation (21).

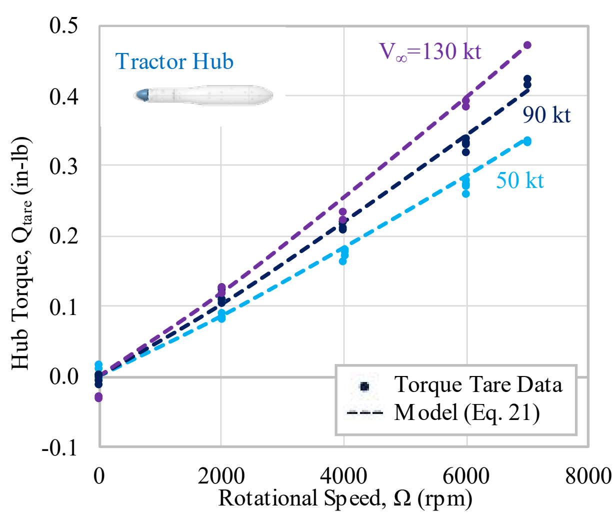

Figure 17. Tractor hub torque tares

6.3 Thrust and Power – Pusher vs Isolated

The blade loading, from both the installed pusher and isolated propeller at 30° collective is shown in Figure 18, plotted against RPM for three wind speeds. At 50 kt, the pusher thrust is nearly the same as the isolated in the lower RPM range but becomes lower at higher RPM. As the wind speed increases, this crossing point is seen to happen at higher rotational speeds.

Figure 19 shows the same blade loading data as in Figure 18 (excluding 70 kt as to not overcrowd the plot) but plotted against the advance ratio instead. For a fixed wind speed, a lower advance ratio corresponds to a higher rotational speed. At a constant pitch and ignoring induced inflow, the advance ratio would be inversely related to the angle of attack on the airfoil sections of the blade. Below about C_T/σ=0.19, the advance ratio has a linear relationship with the blade loading, like the linear region before stall for an airfoil lift vs. angle of attack curve. The rotor then begins to stall beyond about C_T/σ=0.19.

Considering just the isolated thrust first in Figure 19: if induced inflow weren't present, then the advance ratio alone should dictate the blade loading regardless of the wind speed. However, the 90 kt wind speed exhibits a higher blade loading than for 50 kt. This is evidence of induced inflow being present, which is known to reduce with increasing wind speeds per momentum theory. The induced inflow decreases the actual angle of attack on the blade, and because it's smaller at higher wind speed, this explains the higher blade loading at the higher wind speed observed. If instead the x-axis was the ratio of total inflow (freestream plus induced) to the rotational velocity, the blade loadings should be more similar at different wind speeds. However, this is impractical partly because the induced inflow is non-uniform along the blade span.

For the installed pusher propeller in Figure 19: the body impacts the propeller's inflow, while the propeller's induced inflow and interference drag also impacts the body drag, affecting the net thrust of the combined body and propeller. Both effects have been studied in the existing literature. Without measuring the inflow in this test, it's impossible to know exactly how much its effect is causing the results. However, evidence of it can still be observed. At high advance ratios (low thrust), the pusher blade loading is slightly higher than isolated, the effect of which increases with wind speed. This is consistent with a slightly decreased inflow due to the momentum deficit caused by the pusher body. With increasing thrust, the installed pusher thrust (debited by whatever body drag increment is present) gradually decreases relative to the isolated thrust, ultimately erasing the inflow benefit in this case. This is consistent with a gradually increasing body drag increment but could also be due to inflow differences.

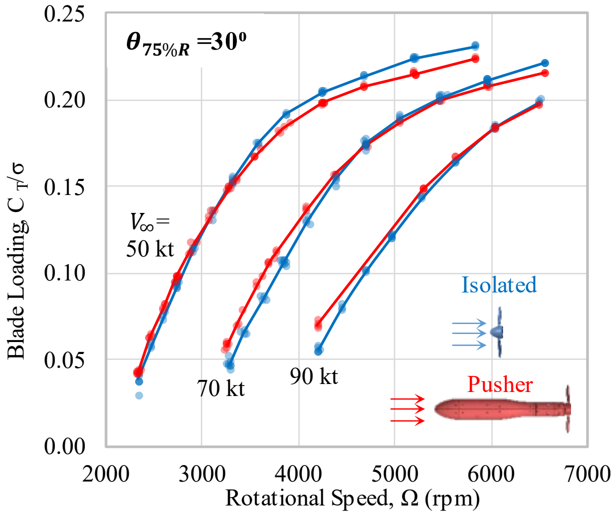

Figure 18. CT/σ vs. Ω @ $\theta_{75\%R}$=30º - Pusher & Iso.

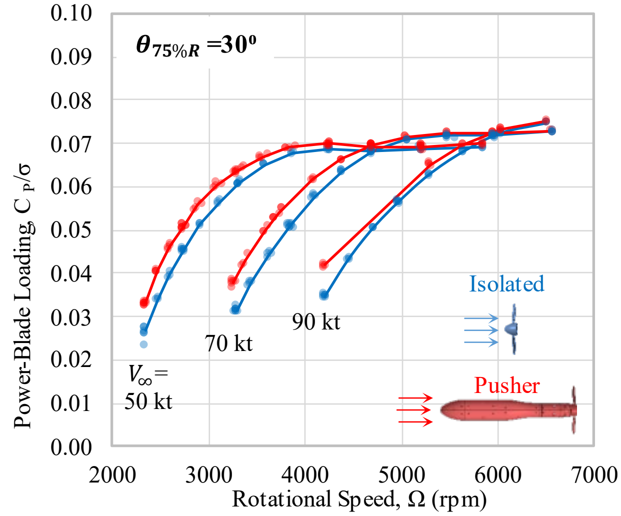

Figure 21. CP/σ vs. Ω @ $\theta_{75\%R}$=30º - Pusher & Iso.

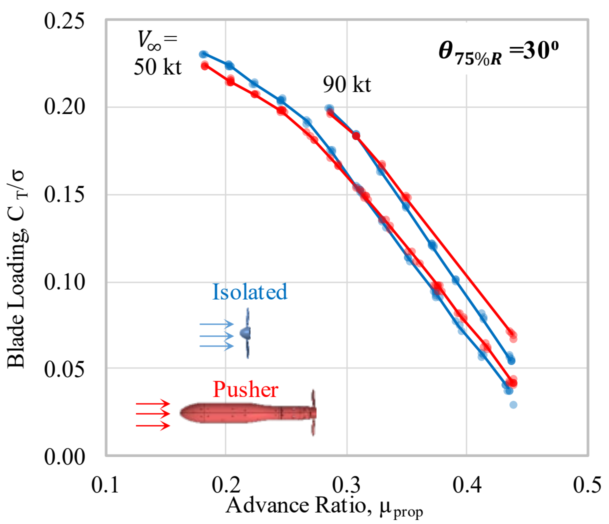

Figure 19. CT/σ vs. μ_{prop} - Pusher & Iso.

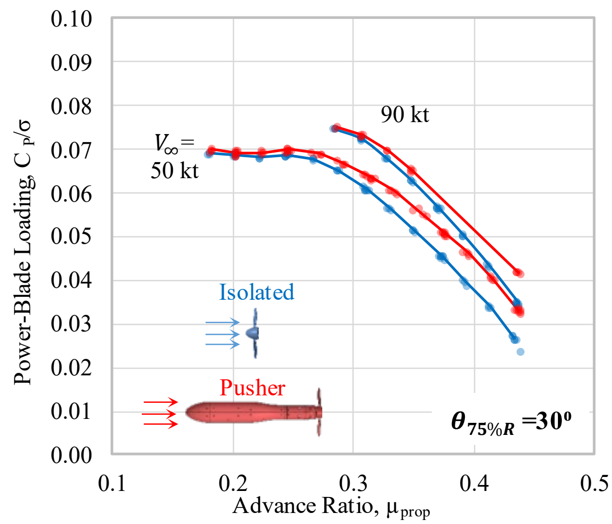

Figure 22. CP/σ vs. μ_{prop} - Pusher & Iso.

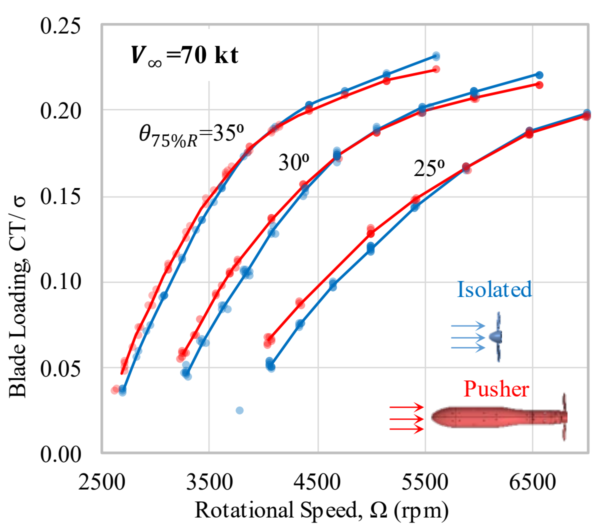

Figure 20. CT/σ vs. Ω @ V_∞=70 kt - Pusher & Iso.

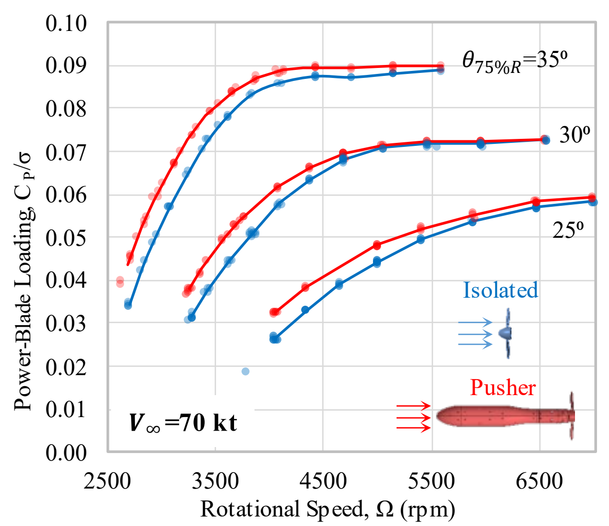

Figure 23. CT/σ vs. Ω @ V_∞=70 kt - Pusher & Iso.

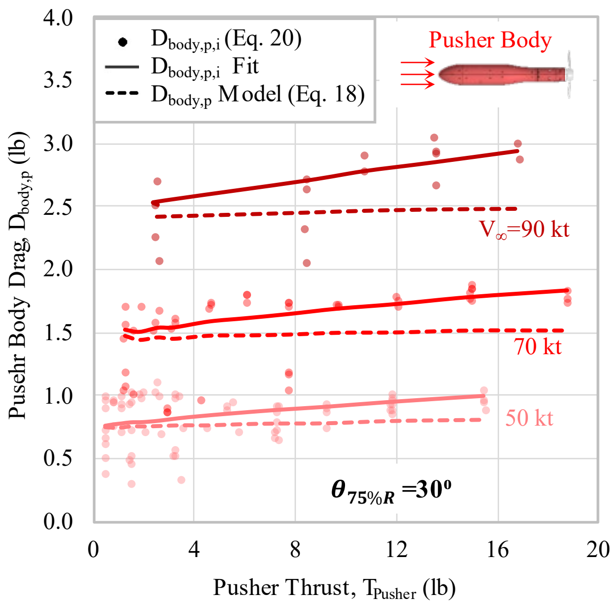

Figure 24. Pusher drag increment and baseline drag

Figure 24 compares the different pusher body drag values to observe the drag increment caused by the propeller. The dashed lines are the baseline body drag calculated with the drag tare model, shown in Figure 16 and described by Equation (18) and (19). The points represent the actual body drag calculated with Equation (20) and the solid lines are best fit curves of this. At lower thrust, there is a lot of scatter in the actual drag data, which improves with increasing thrust. Comparing this data yields a drag increment that gradually increases with increasing thrust. At the highest thrust levels, the absolute value of this drag increment increases with increasing wind speed. However, the higher wind speeds also have higher baseline drag, so the increment appears to increase with some proportionality.

Looking back at Figure 20, it shows the blade loading at 70 kt wind speed for 25º, 30º and 35º collective. Similar trends are seen here compared to the fixed collective at various wind speeds. Observing it from the airfoil's perspective, increasing wind speed at a fixed collective is akin to decreasing the collective at a fixed wind speed.

Figure 21, Figure 22 and Figure 23 show the power-blade loading (C_P/σ) for the same conditions in Figure 18, Figure 19 and Figure 20, respectively. For a fixed pitch, plotted against rotational speed in Figure 21, the C_P/σ curves of different wind speeds cross each other. This consistent with the ideal power in each case, i.e. the product of thrust and wind speed, which is not clearly displayed here when just comparing the C_T/σ and C_P/σ trends shown. Fixing the wind speed, as in Figure 23, makes the thrust and power more proportional to each other because the ideal power is calculated with the same wind speed. Plotting C_P/σ against advance ratio (μ_{prop}) is perhaps the most insightful when comparing it against the blade loading. The product of blade loading and advance ratio is analogous to the ideal power, like the numerator in Equation (36), which can then be compared against the actual power-blade loading.

Even though plotting C_T/σ and C_P/σ against μ_{prop} is useful, it has a couple drawbacks compared to plotting against RPM for a speed-controlled propeller like this. For one, as the thrust increases with RPM by design, plotting it against the advance ratio inverts and skews the relationship, making it less relatable. Second, plotting against advance ratio makes the curves shown in this work much closer together, making it harder to differentiate between them.

6.4 Efficiency – Pusher vs Isolated

The following plots of efficiency are shown with individual data points as transparent circles. Several nominally identical points for each condition were collected, which are used to create the moving averages shown as solid lines. The individual points include data taken after increasing or decreasing the RPM to the setpoint within a run, from different runs with different tunnel temps, and after re-setting the collective pitch. There is not enough data at the same condition to do meaningful statistical analysis. The points indicate the scatter, which is found to be about ±1% efficiency at the peak. This generally improves to about ±0.25% efficiency at max RPM, where the loads are higher in the load cell ranges.

The efficiency, calculated from the isolated and installed pusher thrust in Equation (36), is shown for 30º collective plotted against the blade loading in Figure 25. While it's difficult to distinguish the various curves here, it shows the peak efficiency occurs at a blade loading of roughly C_T/σ=0.14 on average. This is dependent on the collective, with 25º and 30º giving the peak efficiencies at slightly lower and higher, about C_T/σ=0.13 and C_T/σ=0.15, respectively. This is useful to know when observing efficiency plotted against a different variable.

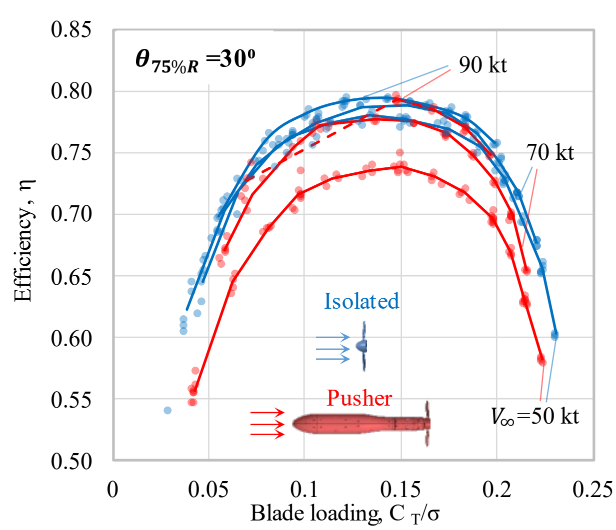

Figure 25. η vs. C_T/σ @ $\theta_{75\%R}$=30º - Pusher & Iso.

The same efficiencies in Figure 25 are plotted against rotational speed in Figure 26. Observing the isolated propeller, the peak efficiency increases slightly with increasing wind speed. This is attributed to the increasing Reynolds number which tends to decrease profile drag. This effect has been observed in other small-scale isolated propeller tests, including Reference 3. Here the 75% radius Reynolds number at the efficiency peaks are $Re_{75\%R}$=144,000, 203,000 and 244,000, for 50 kt, 70 kt and 90 kt, respectively. The corresponding average efficiencies are 78.0%, 78.9% and 79.5%, respectively.

For the installed pusher propeller in Figure 26, the peak efficiency at 50 kt is seen to be nearly 5% below that of the isolated, while at 90 kt the peaks are nearly equal. The dashed portion of the line at 90 kt represents a region where data for the pusher propeller could not be collected due to resonance with the wake of the strut.

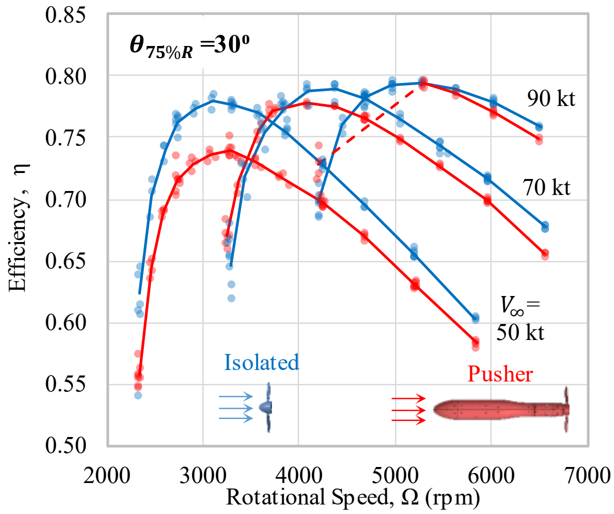

Figure 26. η vs. Ω @ $\theta_{75\%R}$=30° - Pusher & Iso.

Throughout the data set, the pusher propeller peak efficiency is found to be below the isolated at the lower wind speeds, but also increases faster than the isolated with increasing wind speed. This can be observed across Figure 27, Figure 28 and Figure 29, which give the efficiency vs. RPM for the three collectives at 50 kt, 70 kt and 90 kt, respectively. At all three wind speeds, the 30° collective displays the highest peak efficiency for both pusher and isolated. This demonstrates that the differences in inflow, local angle of attack, or other effects, outweigh the Reynolds effect that was seen above.

Starting with the 70 kt data in Figure 28, the pusher at 30° and 25° collective begins to show slightly higher efficiency than the isolated, but only for very low RPM and therefore thrust. This benefit is quickly lost as the RPM increases, before the peak efficiency is reached.

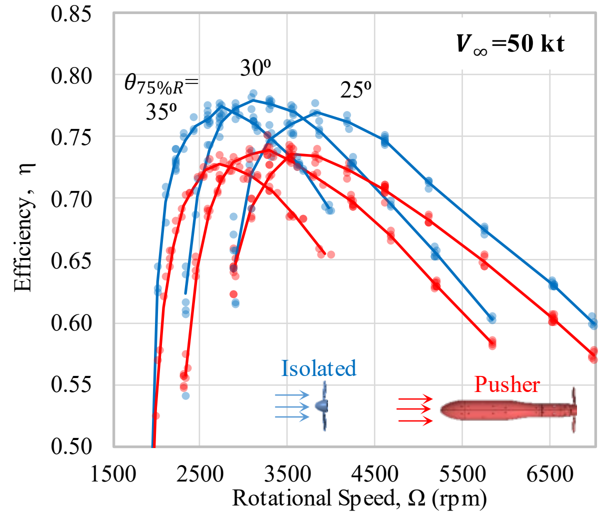

Figure 27. η vs. Ω @ V_∞=50 kt - Pusher & Iso.

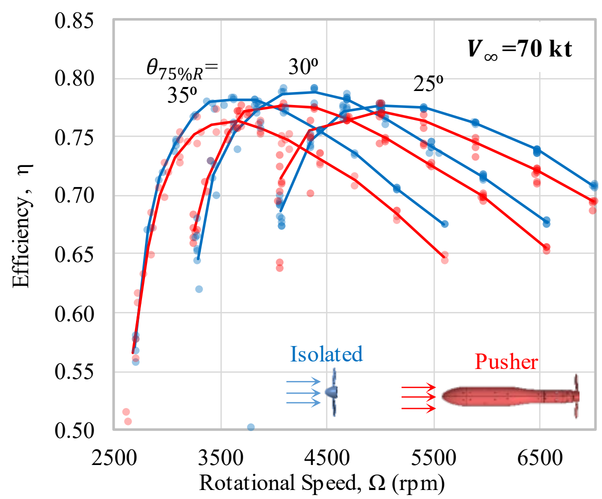

Figure 28. η vs. Ω @ V_∞=70 kt - Pusher & Iso.

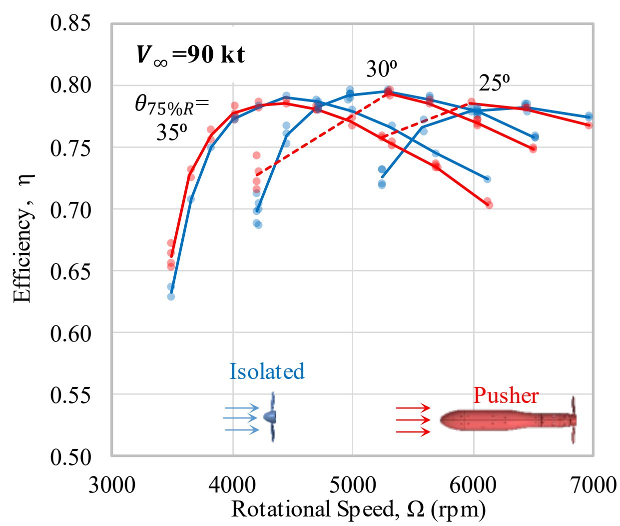

Figure 29. η vs. Ω @ V_∞=90 kt - Pusher & Iso.

For the 90 kt data in Figure 29: again, there are regions where the strut of the wake resonated with the propeller, preventing data collection. This resonance mechanism was not completely dependent on RPM, as the 25º collective resonated at rotational speeds that were not problematic at 30º, and similarly for 30º compared to 35º. This issue was not fully studied or understood. Regardless, the pusher efficiencies at all collectives are higher than the isolated for low RPM, and lower at high RPM. However, the crossing point occurs at a higher RPM than for the lower wind speeds. At 25º collective, the peak pusher efficiency is slightly higher than the isolated and occurs at a lower RPM.

Ultimately, the pusher efficiency is very close to the isolated propeller here. This also suggests that it would out-perform the net performance of a tractor propeller here, if even a small tractor body drag increment was found. The tractor body drag data from Figure 13, albeit for a different body shape (oriented backwards), indicate the increment is not insignificant and can be predicted with basic methods.

Overall, the observed trend is that the pusher efficiency decreases with rotational speed, and therefore thrust, faster than the isolated propeller does. This is consistent with the results of other works, including the results from Sikorsky in Reference 11, which also shows higher pusher efficiencies at lower thrusts. A finding here is that these results can hold true even with different fuselage shapes and sizes relative to the propeller. Also, vastly different propeller designs including different controls (fixed vs variable pitch), blade planform, twist, solidity, number of blades, airfoils, and other considerations such as streamlining the root and propeller hub. Other literature [Ref. 6, 7, 8, 9] suggest results like this weren't guaranteed and depend on several of the factors mentioned. It is unknown if the findings would persist for a complete aircraft configuration, and how other components such as a wing, tail or other drag-creating features would change the results.

7. COMPUTATIONAL RESULTS

CFD analysis was performed using CREATE™-AV Helios [Ref. 15] for the model at 70 kt and 30° collective blade pitch. Helios is a CFD framework for multi-mesh, overset CFD analysis using a variety of solver modules. For this analysis, near-body strand meshes for the blades, hub and test stand are solved using the mStrand solver [Ref. 16], and the off-body mesh is solved using the Cartesian overset solver SAMCart [Ref. 17]. The off-body mesh domain was restricted to the same physical size as the wind tunnel walls in the lateral and vertical directions, with solid inviscid wall boundary conditions specified. The inflow and outflow planes are specified as freestream boundary conditions and extend approximately 10 fairing body lengths forward and aft of the stand.

Fixed adaption of the off-body mesh was made, as seen in Figure 30, with the finest off-body cell corresponding to a size equal to 6.5% thrust-weighted propeller chord for a total of 252M cells. In the near-body, 494 points are used around the airfoil and 223 along the span with clustering set to increase the spanwise density from r/R=0.9 to the tip. The OML of the blade is defined using 17 airfoil cross-sections equally spaced along the span starting from r/R=0.25. This results in a strand mesh of approximately 6M points per blade. Figure 30 also shows the vorticity magnitude for the propeller and stand in the pusher mode operating at 70 kt, 30º collective and 6,000rpm.

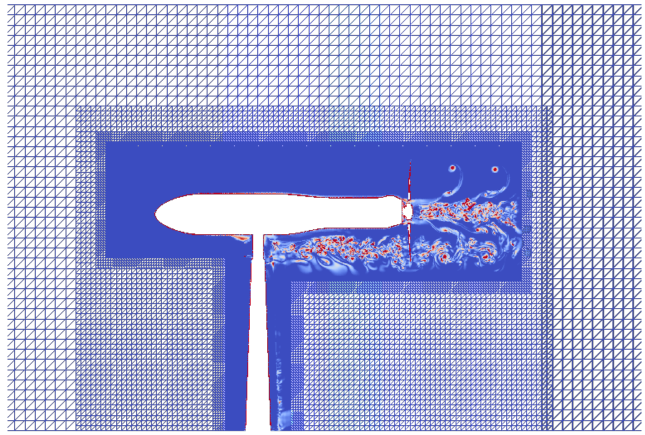

Figure 30. Pusher vorticity magnitude and mesh

Figure 31 shows an iso-contour of the q-criterion colored by vorticity magnitude for the pusher mode at 70 kt, 30º collective and 6,000 rpm. This displays the primary wake of the blade tip vortex as well as the turbulent wake shed by the pylon/stand interface when oriented in pusher mode.

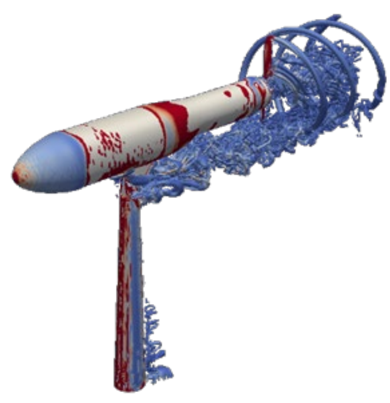

Figure 31. Pusher vorticity magnitude q-criterion

Initial Helios runs were made in both the tractor (isolated) and pusher orientations, both at 70 kt and 30° collective sweeping rotational speed from 3,500-6,500 rpm. Figure 32 through Figure 35 summarize the computational results in comparison with matching experimental data. The Helios results do not debit the pusher thrust by the body drag increment, as the test data does in the experimental results section. In this section, the pusher body drag increment is added back into the test data thrust to provide a more direct comparison with Helios. This does not affect the power. The blade loading and power-blade loading from both Helios and the test data are shown in Figure 32 and Figure 33, respectively.

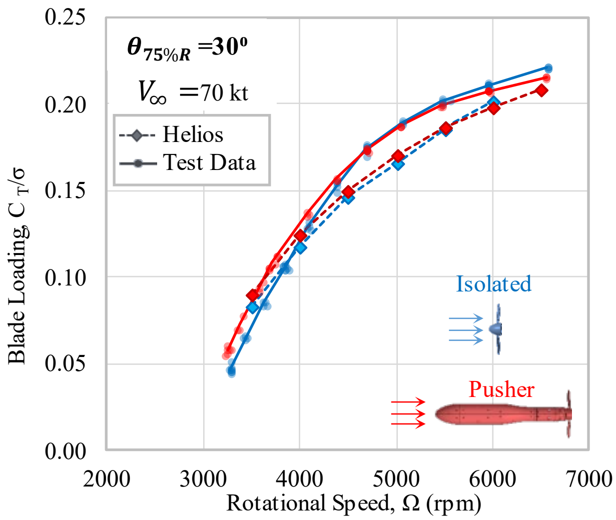

Figure 32. C_T/σ vs. Ω @ Test & CFD

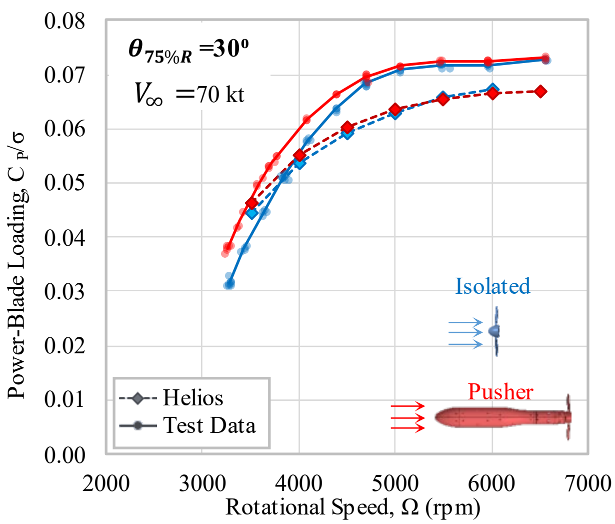

Figure 33. C_P/σ vs. Ω @ Test & CFD

Compared to the test data, the Helios results underpredict thrust for both pusher and isolated over most of the RPM range, but also underpredict the power accordingly. Helios shows similar trends as the test data between the pusher and isolated thrust, with the pusher being higher in the lower RPM range but crossing the isolated at a high RPM.

The efficiencies from the test data and Helios are shown for isolated and pusher in Figure 34 and Figure 35, respectively. These are plotted separately to clearly highlight the differences between the CFD and test data.

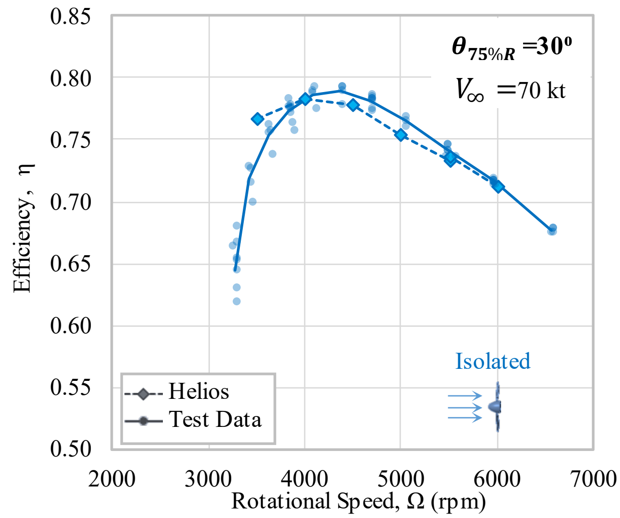

Figure 34. η vs. Ω @ Test & CFD – Isolated

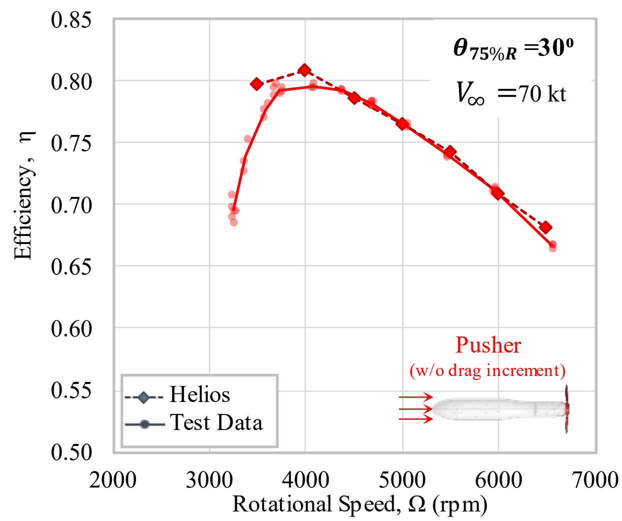

Figure 35. η vs. Ω @ Test & CFD – Pusher

The peak pusher efficiency (without the drag increment) is found to be higher than the isolated at the peak but decreases faster with increasing RPM than the isolated in both the test data and Helios. Helios predicts the efficiency of both configurations to within a couple percentage points and captures the relative changes between the pusher propeller and the isolated propeller.

8. CONCLUSION

This paper summarized the design of the test apparatus, including novel solutions employed to enable to collection of high-quality data, which achieves the goal of experimentally determining the performance of a generic launched effects UAV fuselage and installed pusher propeller. The test was completed in the U.S. Army 7- by 10-ft Wind Tunnel and results were shared for both pusher and isolated propellers. From the data, a few conclusions can be made:

1) The installed pusher propeller thrust (including a body drag increment) exceeds that of the isolated in the lower rotational speed and thrust range but crosses and falls below the isolated thrust at high rotational speeds. The rotational speed and thrust of this crossing point tends to increase with wind speed.
2) The power of the pusher propeller exceeds that of the isolated, but this excess decreases with increasing rotational speed and thrust.
3) The efficiency of the installed pusher propeller may exceed that of the isolated, particularly in regions of lower rotational speed and thrust, but decreases faster than the isolated with increasing thrust.
4) The peak efficiency of the installed pusher propeller increases with wind speed, more so than seen for the isolated propeller. At the lowest wind speed shown, the installed pusher propeller efficiency shows a deficit of about 5% compared to isolated propeller but nearly meets or exceeds the isolated propeller efficiency (depending on pitch) at the highest wind speed.
5) While the Helios results generally underpredict thrust, the predicted power is lower accordingly and the general trends are captured. Importantly, the efficiencies are predicted by Helios to within a couple percentage points of the experimental data, indicating that Helios captures the changes between the pusher and isolated propellers.

While many objectives of this work are complete, there is still future work that can be pursued. This includes flow visualization techniques and wake measurements to better understand the inflow effects observed. Other changes could be explored to further improve the accuracy of the propeller load cell thrust measurement. There is also potential to add more aircraft components to the test model and explore their effects on the results. While the initial Helios results were a step towards validating the CFD methodology, more exploration of the flow field and aerodynamic forces could provide a better understanding of the underlying physics and validate the CFD results. Ultimately, the present experimental and computational results give a better understanding of pusher and isolated propeller performance on a generic launched effects UAV fuselage and lay the groundwork for future studies.

9. ACKNOLAGEMENTS

The authors acknowledge and thank members of the US Army 7x10 Wind Tunnel branch, NASA Aeromechanics branch, and others in the US Army Futures Command. The efforts and insights of those made this work possible while sustaining an excellent and enjoyable working environment.

10. REFERENCES

1. PEO Aviation, “Army successfully demonstrates launched effects system,” U.S. Army article, 22 December 2023. URL: https://www.army.mil/article/272675/army_successfully_demonstrates_launched_effects_system (Accessed 07/10/2024).

2. Dantsker, O.D., Caccamo, M., Deters, R.W., and Selig, M.S., "Performance Testing of APC Electric Fixed-Blade UAV Propellers," AIAA Aviation and Aeronautics Forum and Exposition, Chicago, IL, June 2022.

3. Battey, L. and Russell, C., “Wind Tunnel Testing a Small Isolated Folding Propeller,” Vertical Flight Society’s 76th Annual Forum & Technology Display, Virtual, Oct. 6-8, 2020.

4. Zawodny, N. S. and Haskin, H. H., “Small Propeller and Rotor Testing Capabilities of the NASA Langley Low Speed Aeroacoustic Wind Tunnel," 23rd AIAA/CEAS Aeroacoustics Conference, Denver, CO, AIAA Paper 2017-3709, June 2017.

5. Landman, D., Burnette, D. C., Konuk, E. and Baris, E., “Wind Tunnel Test Techniques for Low-Reynolds Number Propeller Performance Enhancement,” AIAA Aviation Forum, Chicago, IL & Virtual, June 27-July 1, 2022.

6. Bateman, H. and Johansen, F. C., "Pressure and Force Measurement on Airscrew-Body Combinations," British Aeronautical Research Committee, Reports and Memorandum #1380, 1930.

7. McLemore, C. H., "Wind-Tunnel Tests of a 1/20-Scale Airship Model with Stern Propellers," NASA Technical Note D-1026, Langley Air Force Base, VA, January 1962.

8. Dunham, D. M., Gentry, G. L., Manuel, G. S., Applin, Z. T. and Quinto, P. F., “Low-speed aerodynamic characteristics of a twin-engine general aviation configuration with aft-fuselage-mounted pusher propellers,” NASA Technical Paper 2763, NASA Langley Research Center, Hampton, VA, October 1987.

9. Godston, J. and Reynolds, C., “Future Prop-Fans - ractor or Pusher,” AIAA/SAE/ASME/ASEE 21st Joint Propulsion Conference, Monterey, CA, July 8-10, 1985.

10. Sinnige, T., Nederlof, R., and Arnhem, N., “Aerodynamic Performance of Wingtip-Mounted Propellers in Tractor and Pusher Configuration,” AIAA Aviation Forum, Virtual, August 2-6, 2021.

11. Moffitt, B., Bowles, P., Joo, J., Min, B.Y., and Wake, B., “Analysis and Testing of Boundary-Layer-Ingesting Pusher Propeller for High Speed Rotorcraft,” AHS International 73rd Annual Forum & Technology Display, Fort Worth, Texas, USA, May 9-11, 2017.

12. Johnson, W., *Helicopter Theor*y, Princeton University Press, Princeton, NJ, 1980, pp. 25-33.

13. Smith Jr., L. H., “Wake Ingestion Propulsion Benefit,” AIAA/ASME/SAE 27th Joint Propulsion Conference, Sacramento, CA, June 24-27, 1991.

14. Sinsay, J. D., Battey, L. and Milligan, A., “Comprehensive Analysis of Single and Coaxial Small UAS Propellers in Axial Forward Flight,” 49th European Rotorcraft Forum, Bückeburg, Germany, September 5-7, 2023.

15. Sitaraman, J., Hosseinverdi, S., Jude, D., Roget, B., Abras, J., Lakshminarayan, V., and Zagaris G., “Progress in Massively Parallel and Performance Portable Overset Implementations in HPCMP CREATETM-AV Helios,” AIAA SciTech Forum, Orlando, FL, January 2024.

16. Lakshminarayan, V., Wissink, A., Jain, R. and Sitaraman, J., “Improvements to Automated Strand Meshing Capabilities for Rotary Wing Applications,” VFS International Transformative Vertical Flight 2020 Meeting, San Jose, CA, January 2024.

17. Wissink, A., Sitaraman, J., Jayaraman, B., Roget, B., Lakshminarayan, V., Potsdam, M., Jain, R., Leffell, J., Forsythe, J., and Bauer, A., “Recent Advancements in the Helios Rotorcraft Simulation Code”, 54th AIAA Science and Technology Forum and Exposition, San Diego, CA., January 2016.